Chapter 4: $NiCo_2O_4$/NiO/MXene as non-precious metal-based anode catalyst for methanol oxidation

4.1 Introduction

In the era of critical energy situation, researchers are pouring in efforts to find efficient energy storage and conversion devices to replace the prevailing fossil fuels. Direct methanol fuel cell (DMFC) is a potential energy conversion device owing to its high conversion efficiency, high power density, low pollutant emission, methanol being the simplest among all other alcohols, etc [1, 2]. On the other hand, performance of DMFC is affected by the sluggish redox reactions on the anode/cathode surface, poisoning of the catalyst surface, etc. Thus, anode catalyst plays a major role in determining more efficient methanol oxidation reaction. High-performances of these anode catalysts are dependent on electrode properties namely, specific surface area, porosity, hydrophilicity, conductivity, interfacial contact, ion diffusion pathway, concentration of surface-active sites, etc. Two-dimensional materials and their nanocomposites possess high surface area with more exposed active sites endowing them with excellent electrochemical properties [1]. Among various two-dimensional nanomaterials, MXenes have garnered attention in the field of supercapacitors, lithium ions batteries, and catalysis [3, 4, 5]. MXene is a 2D material consisting of transition metal carbides and/or nitrides having formula $M_{n+1}X_nT_x$, where M represents the transition metal from group 13-16, X is carbon and/or nitrogen, and T_x represents the surface functional groups [1, 6]. The distinct chemical and electrical properties of MXenes have open vast opportunities to explore, making them exciting candidate in electrocatalysis. Despite of their remarkable advancement, MXene-based electrocatalysts are still in the developing stage. Their performance is lower than non-noble metal and the traditional Pt-based electrocatalysts. Although a number of MXenes have been predicted, only a limited MXenes are experimentally investigated [7]. More studies should be done to discover new MXenes and identify simpler methods of developing MXene based nanocomposites. Self-restacking of MXene sheets causes reduction in its effective surface area which inhibits the insertion of electrolyte ions into the surface of the electrode. In this regard, developing hybrids of MXenes with noble and non-noble metal nanostructures [1, 8, 9], transition metal dichalcogenides [8, 10, 11]; reduced graphene oxide, CNT [1, 11], conducting polymer [12], etc. have performed

better than the pristine components. For instance, Ni is regarded as brilliant choice for electrochemical devices such as energy conversion, storage, etc. because Ni and its alloys may increase the rate of CO oxidation at the active sites of its oxides, thereby resisting CO poisoning. MoS_2, a 2D transition metal dichalcogenide is also resistive to CO poisoning. By doping Ni or any other metal ions into MoS_2, one can achieve higher methanol catalysis as the ions get hybridized inside the 2D layers and increases the ion diffusion pathways. The methanol oxidation current density improves significantly on making a composite of this Ni doped MoS_2 with MXene attributed to the synergistic effects of low onset potential of Ni, high mechanical stability and conductivity of MoS_2 and MXene respectively [8, 9]. In another work, $Ti_3C_2T_x$ and graphene oxide nanosheets were designed to form a porous three-dimensional cross-connected nanostructure being covered with Pd nanoparticles (NPs). Formic acid oxidation is further increased by the strong interaction between Pd NPs and $Ti_3C_2T_x$, which decreases the CO adsorption on the Pd active sites. Furthermore, lower charge transfer resistance of the nanocomposite is because of the 3D network, which offers numerous channels for redox reactions to occur. These numerous channels increase the triple-phase boundaries, which improves the oxidation of formic acid [1]. Conducting polymers are also explored with MXene in energy devices. When combined with Pd, polyaniline (PANI) gives rapid electron transfer kinetics and exceptional electrode stability. Pd/PANI when composited with MXene, performs even better as the surface of MXene couples with the transition metal lattice to facilitate interfacial electron transfer and lattice mismatch [12]. However, the study of MXene based non-noble metal electrocatalyst in DMFC is in a nascent stage, which needs to be explored.

In this chapter, a nanocomposite based on hybridization of MXene nanosheets with binary mixed metal oxide $NiCo_2O_4$/NiO is developed as anode catalyst for methanol oxidation. It is expected that the high corrosion resistance of these binary metal oxides in synergy with their interfacial interaction with layered MXene structures, will facilitate more penetration of electrolyte ions into the electrode. The conductivity of $NiCo_2O_4$ is about two-fold that of pristine metal oxides Co_3O_4 and NiO. Thus, the binary metal oxide $NiCo_2O_4$/NiO is developed to compensate the low conductivity and to achieve synergistic effects of the individual transition metal oxides. Moreover, the restacking of MXene sheets is resolved by developing the hybrid with $NiCo_2O_4$/NiO. These metal oxides

provide plenty of redox sites which in synergy with the high surface area, hydrophilicity of MXene lead to enhanced electrocatalytic activity of the nanocomposite.

The supercapacitive performance of this developed nanocomposite will be studied in chapter 6.

4.2 Experimental section

4.2.1 Material synthesis

4.2.1.1 Synthesis of $NiCo_2O_4$/NiO/MXene (CNOT): 0.5 g of MAX phase (Ti_3AlC_2) was added slowly to 30 ml of etchant (2M NH_4HF_2) and the solution was left to stir for 24 hours at room temperature. The reaction product was washed with distilled water and ethanol until the pH becomes neutral. The resulting slurry was dried in a drying oven for 12 hours at 80° C. The MXene nanosheets were obtained thereafter by dispersing the etched MXene in distilled water and sonicating for few hours in a nitrogen environment to prevent oxidation of the MXene nanosheets [13]. The hybrid $NiCo_2O_4$/NiO/MXene (CNOT) is synthesized by sonication-assisted mixing to develop a homogeneous solution of binary mixed metal oxide composite $NiCo_2O_4$/NiO with MXene. The synthesis of $NiCo_2O_4$/NiO (CNO) and $NiCo_2O_4$ (NCO) are done by following the methods explained in section 3.2.1.1 of chapter 3.

4.2.2 Material characterizations:

X-Ray Diffraction was carried out by using X-ray diffractometer, Make-Bruker Axs of Germany, Model-D8 Focus. Fourier transform infrared (FTIR) spectroscopy analysis was done to study the chemical structures of the samples (PerkinElmer spectrometer, Model: Frontier MIR FIR) and for X-Ray Photoelectron Spectroscopy (XPS) by Thermo Fisher Scientific Pvt. Ltd. of UK, Model-ESCALAB Xi^+ was employed. The morphology of the samples was observed by Transmission Electron Microscopy (TEM) (TECNAI G2 20 S-TWIN) and Field emission scanning electron microscopy (FESEM) (Model: Zeiss, Sigma). BET was done to study the surface and pore size analysis (Anton Paar, Autosorb iQ MP-AG (2 STAT)).

4.2.3 Electrochemical characterizations:

Electrochemical studies were conducted using three electrode and two-electrode system in Gamry (Model- Gamry Interface 1010 E) at ambient environment. Pt wire (counter), Ag/AgCl (Reference) and glassy carbon electrode (GCE of 0.5 cm diameter) coated with sample (working electrode) were used for the three-electrode study. Catalyst slurry was prepared by mixing the active material, carbon black and nafion in the ratio of 75:15:10 in isopropanol and DI water. The electrochemical characterizations were performed in 0.5 molar sodium hydroxide aqueous electrolyte. Performances of the electrodes were evaluated by performing cyclic voltammetry (CV), chronoamperometry (CA), and electrochemical impedance spectroscopy (EIS). Potential window of -0.2 to +0.65 V was considered for cyclic voltammetry. CA was performed at 0.65 V for 1 hr. EIS was performed in frequency range 0.1 Hz - 1 MHz with constant amplitude of 10 mV.

All the structural and electrochemical characterizations of pristine metal oxide $NiCo_2O_4$ (NCO) and $NiCo_2O_4$/NiO (CNO) are discussed in chapter 3. This chapter contains basically the study of the nanocomposite CNOT.

4.3 Results and Discussion

4.3.1 Morphological characterizations

The porous nature of the nanocomposite CNOT is prominent from the FESEM images in fig. 4.1a. The removal of Al layers from the Ti_3AlC_2 layers leads to the increase in distance between the layers of MXene, which is clearly visible from fig. 4.1b. The removal of aluminium can also be inferred from the minimum Al concentration in EDX spectra shown in fig. 4.4. As observed from the TEM images in fig. 4.1c and 4.1d, the $NiCo_2O_4$/NiO nanoparticles are uniformly dispersed on the MXene nanosheets. From the HRTEM image in fig. 4.2a, lattice d-spacing of 0.25 and 0.48 nm are observed which correspond to (311) and (111) plane of $NiCo_2O_4$. On the other hand, lattice spacing of 0.5 nm is found which occurs due to (0004) plane of MXene [14]. The SAED pattern of CNOT in fig. 4.2b confirms the presence of different planes (222), (400), (422), (533) planes of $NiCo_2O_4$ with calculated d-spacing 0.245, 0.206, 0.177, 0.127 nm respectively, and (400), (511) planes of NiO with d-spacing 0.104, 0.082 nm respectively [15, 16]. Fig. 4.2c shows the particle size distribution of the $NiCo_2O_4$/NiO particles in fig. 4.1d and the average size is calculated to be 67.5 nm.

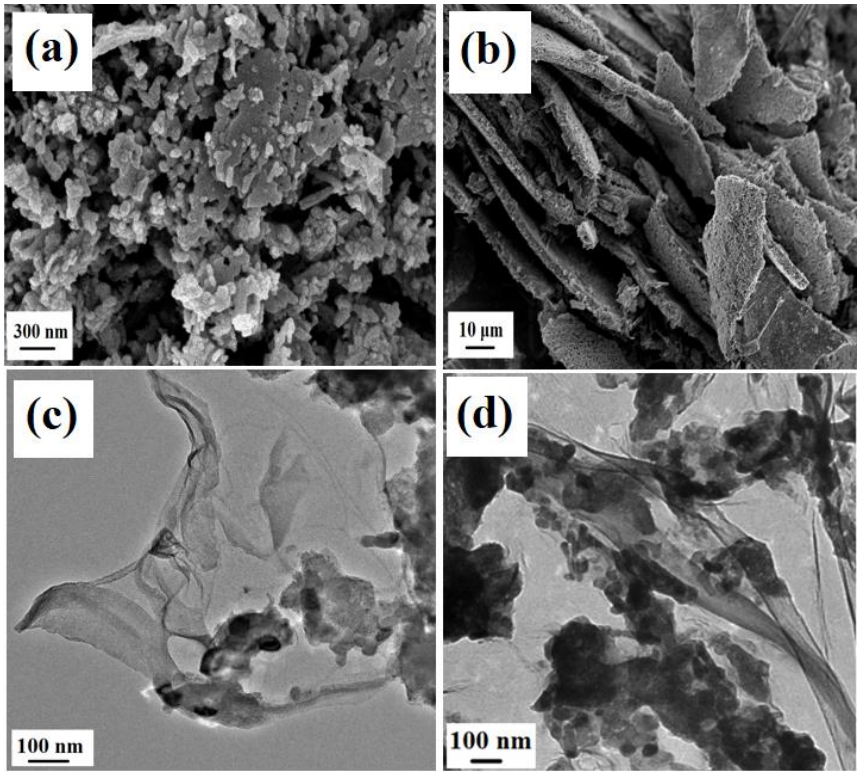

Figure 4.1: Morphological characterizations of CNOT: (a)-(b) FESEM images, (c)-(d) TEM images

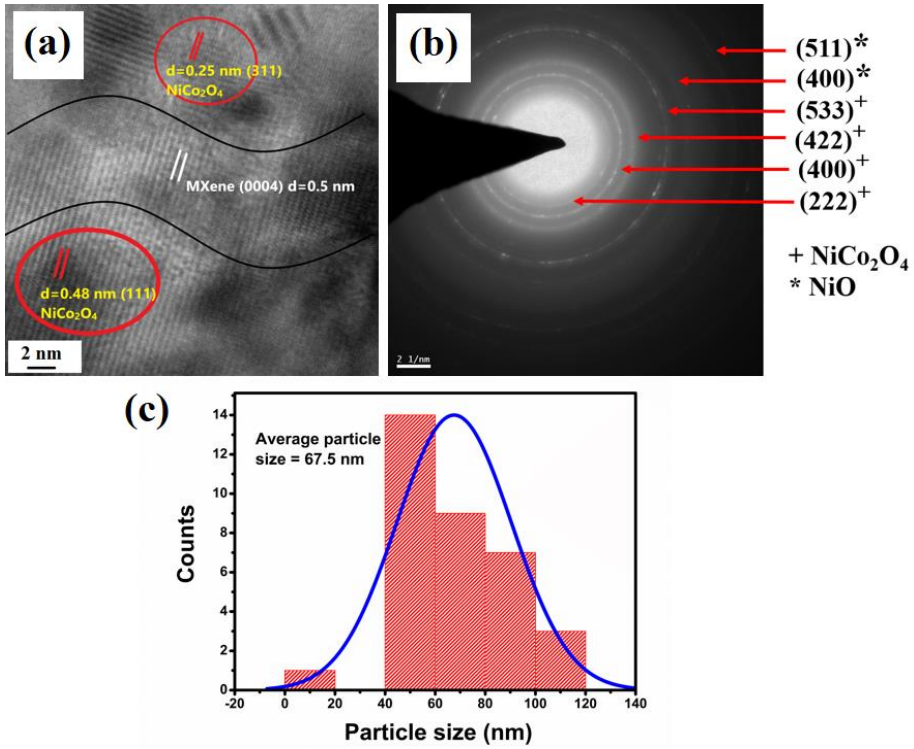

Figure 4.2: Morphological characterizations of CNOT: (a) HRTEM image with d-value, (b) SAED pattern, (c) Particle size distribution of CNO in CNOT

Figure 4.3a displays the SAED pattern of $NiCo_2O_4$, which confirms the presence of different planes (111), (220), (222), (331), (422), (511), (440), (533), (800) with calculated d-spacing 0.45, 0.279, 0.238, 0.198, 0.161, 0.15, 0.138, 0.12, and 0.101 nm respectively [15, 16]. Nanoflake morphology of NCO is evident from fig. 4.3b. At higher magnification TEM image of NCO in fig. 4.3c, the grains are observed whose average size is calculated to be 17.6 nm as shown by histogram in fig. 4.3d.

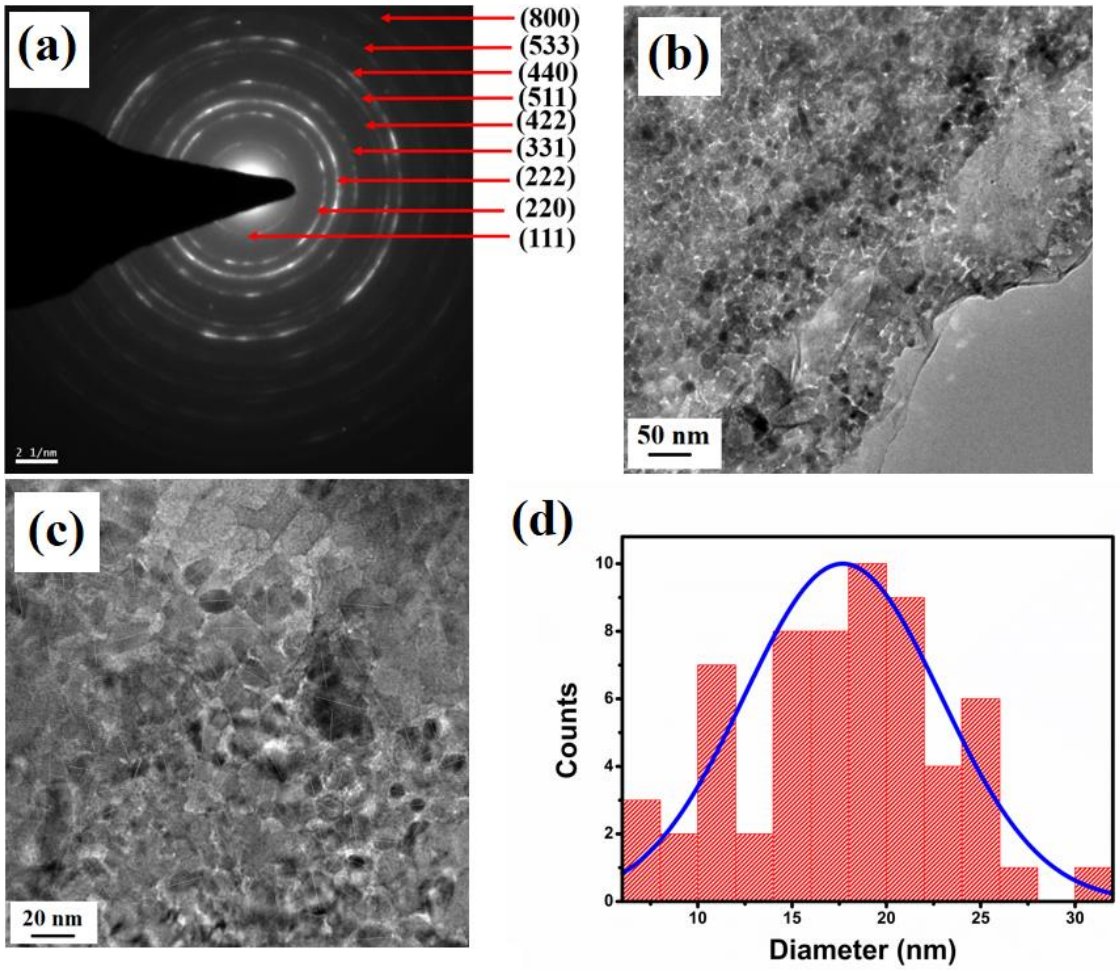

Figure 4.3-: Morphology of NCO: (a) SAED pattern, (b)-(c) HRTEM images, (d) Grain size distribution of NCO

The EDX spectra of MXene in fig. 4.4a confirms the presence of O and F terminations on MXene surface. The aluminium, fluorine and nitrogen observed may arise because of the formation of the by-products AlF_3, and $(NH_4)_3AlF_6$ during the etching process, which also corroborates well with the XRD pattern. The presence of the required elements of CNOT can be observed from the EDX spectra of CNOT in fig. 4.4b.

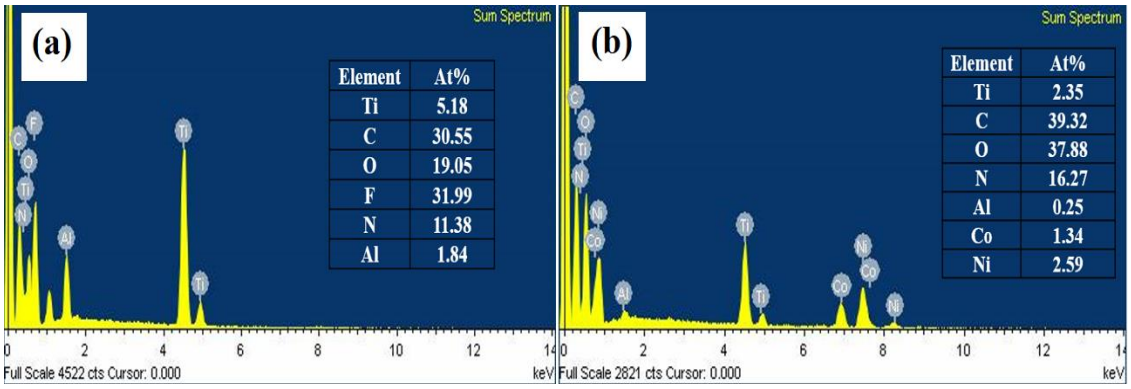

Figure 4.4: EDX spectra: (a) Etched MXene, (b) CNOT

4.3.2 Physical characterizations

4.3.2.1 X-ray Diffraction (XRD)

The formation of MXene and diminishing of MAX phase is confirmed from the disappearance of the XRD peak corresponding to (104) plane of Ti_3AlC_2, as shown in fig 4.5a(i) [13]. In MXene, the peak corresponding to (002) plane of Ti_3AlC_2 gets shifted from 9.53° to 7.1°, which further confirms the formation of MXene from MAX phase. Additional peaks appearing at 28.3°, 34.3°, and 61° represent the (006), (101), and (110) plane of Ti_3C_2 [13]. Two additional MXene peaks are observed at 72° and 76.3° [17]. The production of by-products during the etching process can also be identified by their XRD peaks. The peaks at 25.5°, 40.6° correspond to AlF_3 and peaks at 35.8°, 41.6°, 54.8° are attributed to product $(NH_4)_3AlF_6$ [13]. After delamination of MXene, the interplanar spacing between (002) plane increases further which is confirmed by the shift of 7.1° peak to 6.83° as depicted in fig. 4.5a(ii). The XRD spectrum of CNOT in figure 4.5a(iii) displays the characteristic diffraction peaks of $NiCo_2O_4$ at 18.6˚, 31.3˚, 37˚, 54˚, 59.5˚, and 65.2˚ corresponding to (111), (220), (311), (422), (511), and (440) planes respectively [18]. The diffraction peaks corroborate well with the JCPDS (No- 73-1702) pattern for face-centered cubic $NiCo_2O_4$ with spinel structure. Diffraction peaks at 43.3˚,62.6˚,75.5˚, and 79˚correspond to (200), (220), (311), and (222) planes of NiO (JCPDS No- 73–1519) [19]. The crystal structure formation of $NiCo_2O_4$/NiO is confirmed as all the planes corresponding to $NiCo_2O_4$ and NiO are observed.

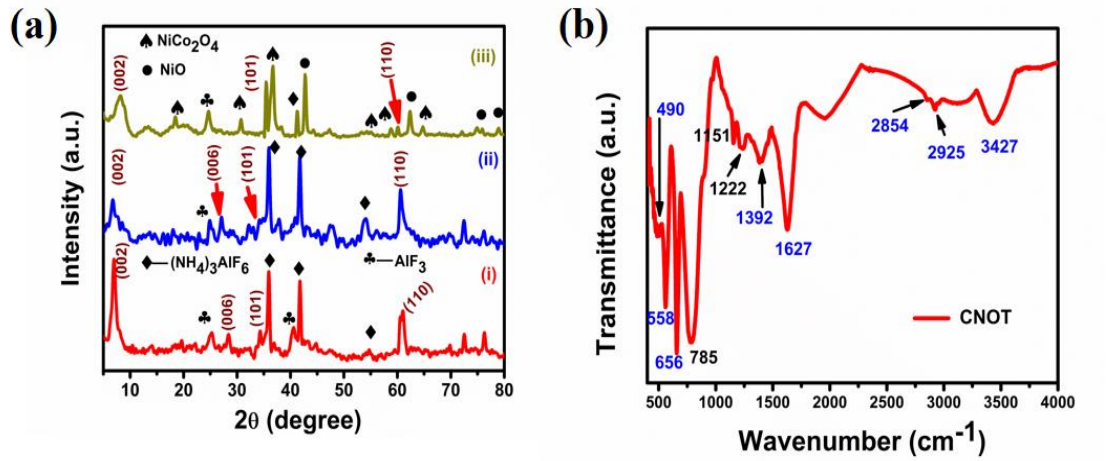

Figure 4.5: (a) XRD of (i) MXene, (ii) delaminated MXene, (iii) CNOT, (b) FTIR of CNOT

4.3.2.2 Fourier transform infrared spectroscopy (FTIR)

In FTIR spectra of CNOT in fig. 4.5b, the vibrational band observed at 490 cm^{-1} is due to overlapping of Ni-O antisymmetric stretching vibrations of NiO, along with Ti-C bond of MXene. Similarly, the absorptions occurring at 656 cm^{-1} is due to contribution from Ni-O bond and Ti-O bond respectively. The absorption peak at 558 cm^{-1} correspond to Co-O stretching vibration of $NiCo_2O_4$. The vibrational bands at 1392, 1627, 2854, 2925, and 3427 cm^{-1} correspond to C-O bond, bending mode of H_2O molecule, symmetric and asymmetric CH_2 stretching, and O-H stretching mode of water molecule respectively. Additional absorption peaks are situated at 785 and 1151 cm^{-1} which correspond to Ti-F and C-F bond respectively [20]. The absorption at 1222 cm^{-1} occurs due to the bending mode of water molecules. Thus, from FTIR spectra the presence of different surface terminals i.e., -F and -O can be concluded.

4.3.2.3 Nitrogen (N_2) adsorption-desorption analysis

N_2 adsorption-desorption curve is obtained using Brunauer–Emmett–Teller method. As presented in fig. 4.6, CNOT exhibits fourth class of isotherm along with H3 hysteresis, confirming mesoporous structure. Due to its porous surface, CNOT offers high specific surface area of 86.8 m^2/gm. Average pore size of around 3.4 nm is obtained using Barrett–Joyner–Halenda method. From calculation, CNOT is found to be 50 % porous.

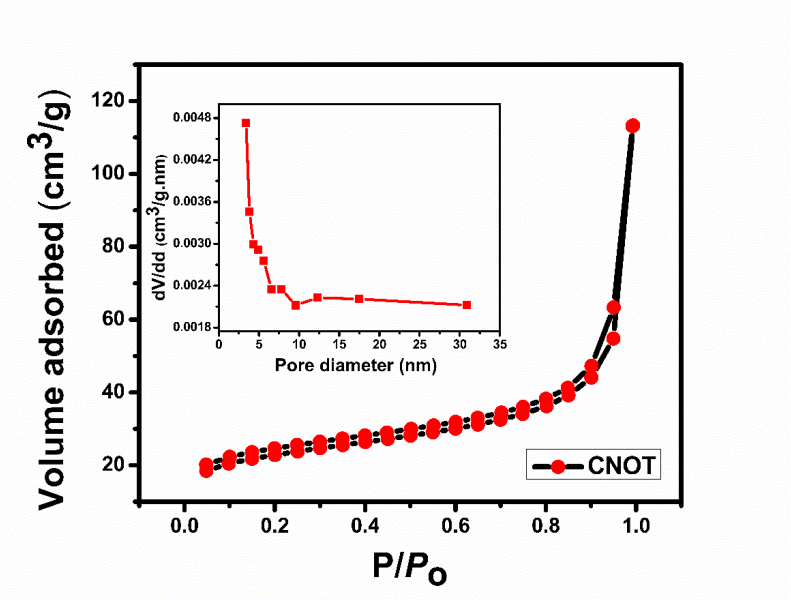

Figure 4.6: N_2 adsorption-desorption isotherms of CNOT. Inset-Pore size distribution curve

4.3.3 Electrochemical characterizations

4.3.3.1. Electrochemical activity of the electrodes in absence of methanol

To understand the electrochemical behaviour of the catalyst CNOT in alkaline medium, cyclic voltammetry is performed in 0.5 M NaOH aqueous solution. From the CV profile of CNOT presented in fig. 4.7a, a pair of redox peaks is observed, which correspond to the change in oxidation states of Co (Co^{2+}/Co^{3+}) and Ni (Ni^{2+}/Ni^{3+}). The redox reaction behind the peaks can be expressed as: $NiCo_2O_4 + OH^- + H_2O \rightarrow 2CoOOH + NiOOH + e^-$. With increase in scan rate, the anodic peak shifts towards higher side, whereas the cathodic peak shifts to lower value, indicating the quasi-reversibility of the electrochemical reactions taking place on the electrode surface. Peak-to-peak separation (ΔE_p) of 25.62 mV obtained at 10 mV/s scan rate, represents good reversibility of the electrode CNOT at low scan rate. This separation increases to 132.6 mV on reaching 200 mV/s scan rate, which implies quasi reversibility of the electrode material at higher scan rate. The good reversibility of the hybrid electrode CNOT arises due to- (i) conductivity of the hybrid, (ii) pores on the electrode, which facilitate quick and facile charge transfer. The peak current density (I_p) varies linearly with scan rate (v) (fig. 4.7b) and square root of scan rate (fig. 4.7c), suggesting presence of both mechanisms surface-controlled and diffusion-controlled reaction of CNOT. The presence of both these processes in the electrode is further confirmed by the slope of log I_p vs log v (shown in fig. 4.7d) equal to

0.6. The concentration of surface adsorbed species can be calculated using Brown-Anson Model.

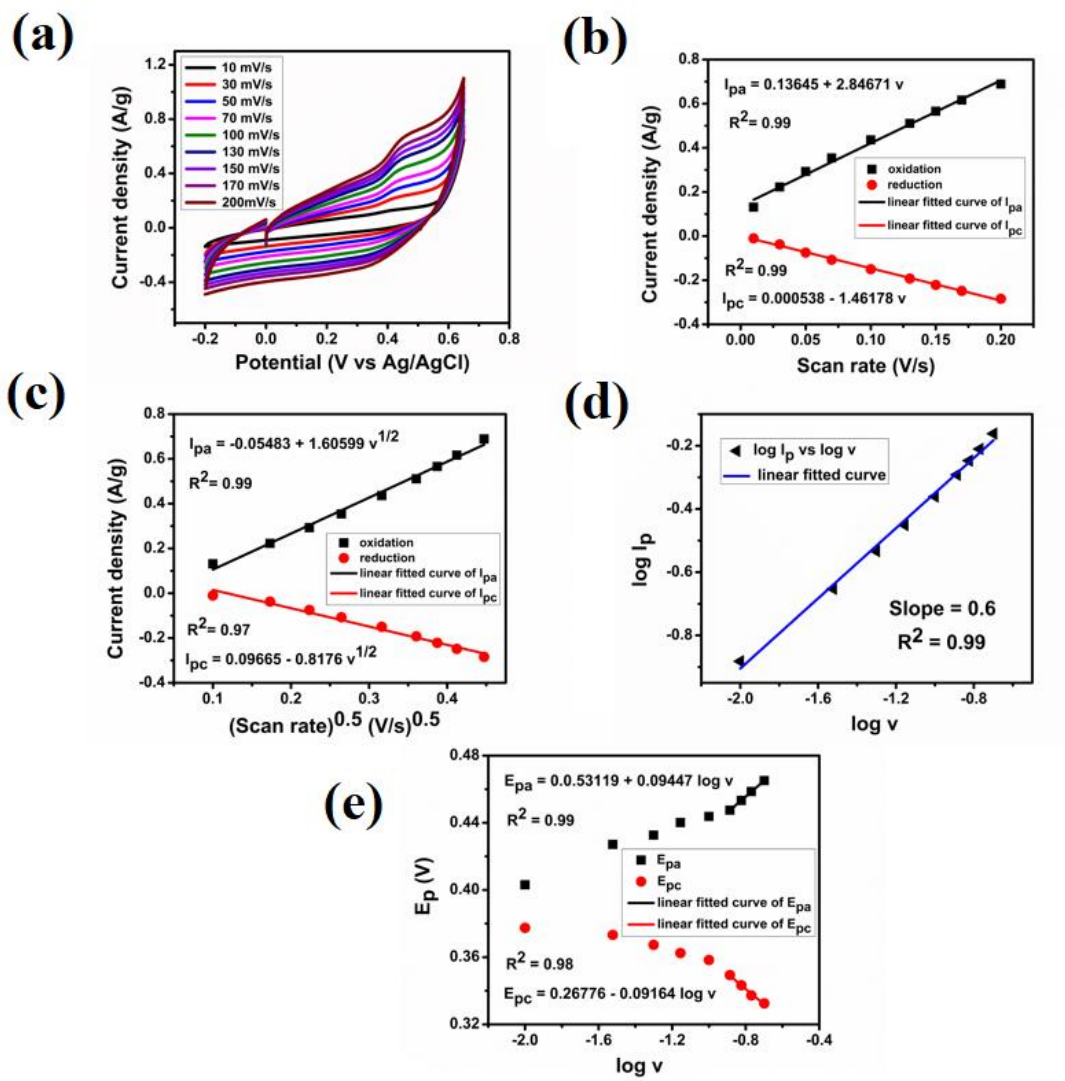

Figure 4.7: (a) Cyclic voltammetry of CNOT/GC in 0.5 molar sodium hydroxide, Plot of (b) I_p vs. ν, (c) I_p vs. $\nu^{1/2}$, (d) log I_p vs log ν, (e) Laviron's plot: Anodic and cathodic peak potential (V) vs logarithm of scan rate of CNOT

According to Brown-Anson Model, $I_p = \frac{n^2F^2}{4RT}\nu A\Gamma^*$ where, I_p signifies the peak current density, n denotes the number of transferred electrons, F is the Faraday constant, ν is the sweep rate, A signifies the area of the electrode, Γ^* is the surface coverage of the adsorbed species in mol/gcm^2 [21], R and T represent the gas constant and absolute temperature, respectively. The surface adsorbed redox species of CNOT is calculated using Brown-Anson Model and found to be 1.5 ×10^{-5} mol/gcm^2. The high value of surface adsorbed

redox species of CNOT in comparison to reported works, suggests good electrochemical activity of the catalyst. The kinetics of the catalyst is understood by using Laviron's equation which gives electron transfer coefficient (α) and heterogeneous rate constant (k_s) [13]. The Laviron's equations are written as-

$E_{pa} = E_o + 2.3\ RT\frac{\log \nu}{(1-\alpha)nF}$, $E_{pc} = E_o - 2.3RT\frac{log\nu}{\alpha nF}$ and

$logk_s = \alpha \log(1-\alpha) + (1-\alpha)log\alpha - log\frac{RT}{nF\nu} - \frac{\alpha(1-\alpha)nF\Delta E_p}{2.3RT}$

where E_{pa} and E_{ca} are the anodic and cathodic peak potentials, respectively, n is the number of electrons transferred, E_o represents formal potential, and other terms represent their traditional meanings. From the slope of plot E_p vs log ν (shown in fig. 4.7e), the electron transfer coefficient (α) of catalyst CNOT is found to be 0.37 and average heterogeneous rate constant (k_s) is calculated to be 0.9 s^{-1}. The high heterogeneous rate constant implies excellent electrochemical performance of the hybrid CNOT in alkaline electrolyte.

4.3.3.2 Electrochemical activity of the electrodes in presence of methanol

On adding methanol to the 0.5 M NaOH solution, an abrupt increase in anodic current is observed, which is because of the oxidation of methanol. In figure 4.8a, the methanol oxidation in presence of different methanol concentration is observed at 10 mV/s scan rate. Methanol oxidation current density of 15 A/g with low onset potential of 0.30 V vs. Ag/AgCl is obtained for CNOT electrode at 5 M methanol concentration. The current density of CNOT is higher than the pristine NCO and binary electrode CNO (discussed in section 3.3.3.2 of chapter 3), due to the interfacial interactions between MXene nanosheets and $NiCo_2O_4$, NiO. The presence of MXene nanosheets provide hydrophilicity and conductivity to the nanocomposite CNOT. At higher methanol concentration higher than 5 M, the active sites get impassable and the methanol oxidation cannot be increased further. So, keeping the concentration 5 M constant, the effect of scan rate is studied by changing the scan rate from 10-200 mV/s (shown in fig. 4.8b). With increase in scan rate, the methanol oxidation current decreases, which is because of the quasi-reversibility of the oxidation reaction. Moreover, with increase in scan rate, the increase in cathodic peak current corresponding to Co^{3+}/Co^{2+} and Ni^{3+}/Ni^{2+} conversion corroborates well with the reduction of methanol oxidation with scan rate. The probable chemical reactions involved in methanol oxidation are as follows (equations 4.1-4.2):

$$NiOOH + CH_3OH + 1.25O_2 \rightarrow Ni(OH)_2 + CO_2 + 1.5H_2O \quad (4.1)$$

$$2CoOOH + 2CH_3OH + 2.5O_2 \rightarrow 2Co(OH)_2 + 2CO_2 + 3H_2O \quad (4.2)$$

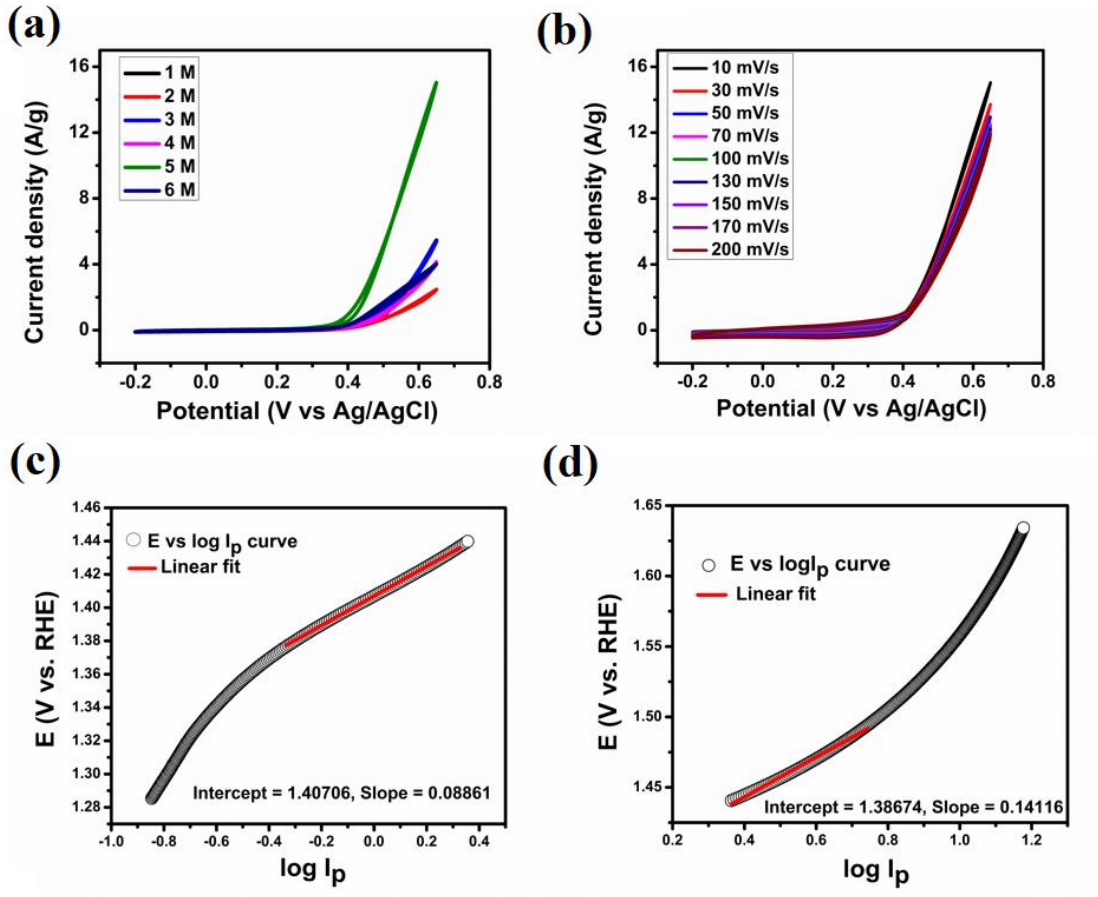

Figure 4.8: Cyclic voltammetry in presence of methanol: (a) different concentration of methanol at 10 mV/s, (b) 5 M methanol concentration, Tafel plots of CNOT/GC in 5 M methanol at 10 mVs^{-1}, (c) low overpotential, (d) high overpotential

Tafel equation helps understanding the kinetics of methanol oxidation. Tafel equation is expressed as $E_p = \frac{2.303\,RT}{\alpha nF}[logI_p - logI_o]$ where, E_p is the overpotential given by (E-E_{eq}), E represents the operating potential, E_{eq} is the equilibrium potential; I_p represents the methanol oxidation current density, I_o is the exchange current density, α and F represent electron transfer coefficient and Faraday constant, respectively [22]. From the Tafel plot of CNOT/GC as shown in fig. 4.8c, 4.8d, it is observed that the electrode behaves differently at low and high overpotential values. At working potential lower than 0.45 V vs. Ag/AgCl, a lower Tafel slope of 88.6 mV/dec is obtained, whereas at potential higher than that, a higher Tafel slope of 141.16 mV/dec is obtained. The different Tafel

slopes signify that the methanol oxidation reaction has different rate determining step at these potentials [23, 24]. The lower Tafel slope suggests higher methanol dehydrogenation at lower potential; whereas at higher potential, the electrode surface gets adsorbed by CO intermediates. So, oxidation of these CO becomes the rate determining step at higher potential. Electron transfer coefficient (α) of 0.667 and 0.41 is obtained at lower and higher potential respectively. Comparatively higher α value signifies higher methanol oxidation at lower potential.

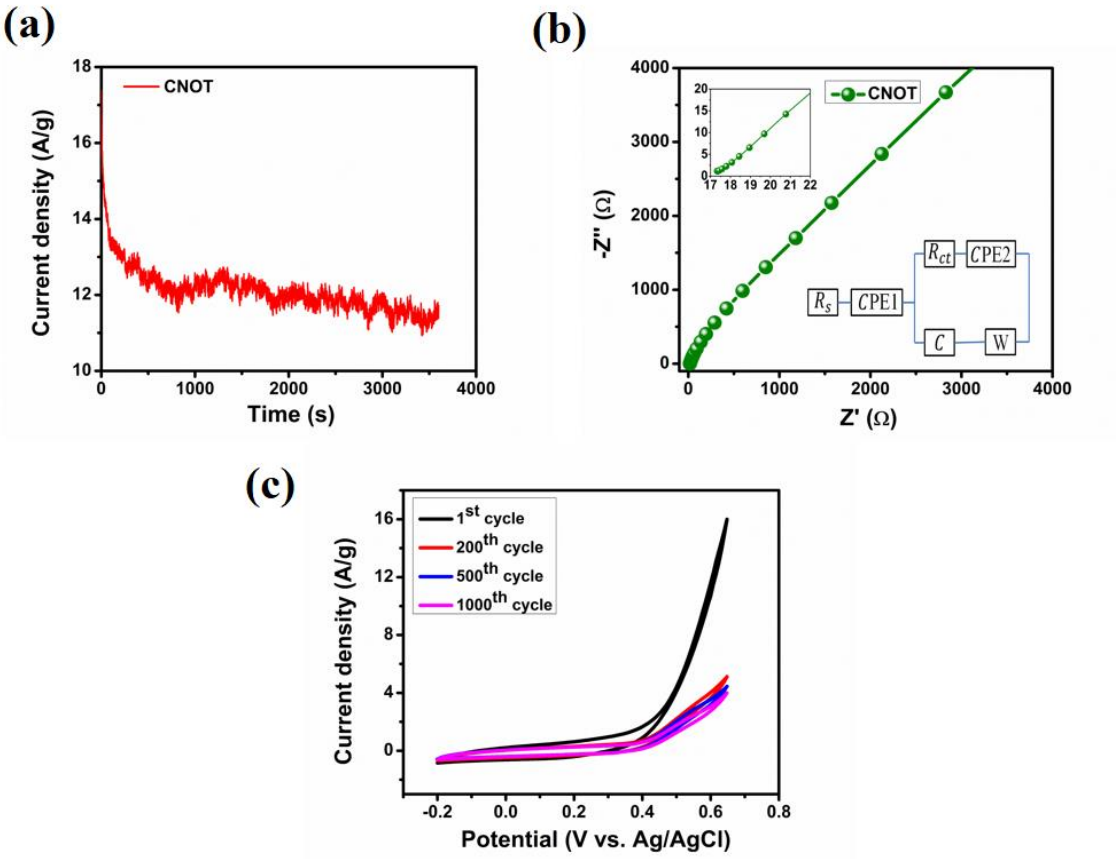

Figure 4.9: (a) Chronoamperometry in 5 M methanol at 0.65 V for 1 hr, (b) Nyquist plot of CNOT in 5 M methanol solution. (Left inset: zoomed image of high frequency region Nyquist plot, Right inset: Equivalent circuit), (c) Cycling stability at 20 mVs^{-1} in 5 M methanol. The supporting electrolyte is 0.5 M NaOH aqueous solution

To understand the electrochemical stability of the electrode, chronoamperometry is performed for one hour at 0.65 V. As shown in fig. 4.9a, the current initially decreases up to 800 s due to formation of CO intermediates and then remains constant for the rest of the time. The CO tolerance of the electrode can be assessed by calculating the

deterioration rate during the interval 800 to 3600 s. 67 % current retention and low deterioration rate of 5.85×10^{-6} s^{-1} obtained for CNOT/GC confirms the durability of the electrode, which is found to be durable than many carbon-based catalysts [25, 26]. The hydrophilic terminations on MXene surface react with the adsorbed CO intermediates, thereby releasing the active sites. Thus, it increases the lifetime of the electrode. The charge transfer resistance offered by CNOT in 5 M methanol solution containing 0.5 M NaOH is assessed by Nyquist plot as shown in fig. 4.9b. The small diameter of the semicircle suggests low charge transfer resistance (4.46 Ω) offered by the electrode. The high surface area, available hydrophilic terminations, presence of multiple active sites contribute to charge transfer. The stability of the electrodes is studied by observing the cycling stability of the electrode CNOT/GC for about 1000 CV cycles in 5 M methanol (fig. 4.9c). Current retention of around 32%, 28% and 25% is obtained after 200, 500 and 1000 cycles. The sudden decrease in MOR current is due to the consumption of methanol molecules and coverage of the active sites with intermediate products. The current retention after 200 CV cycles does not change much which indicates good cycling stability of the catalyst CNOT.

4.3.4 Characterizations of the electrode after cycling stability

The elemental composition and oxidation states of the different metal ions before and after methanol oxidation are confirmed by XPS. The presence of Ni, Co, O, Ti, C as the main constituting elements is confirmed from the survey spectra shown in fig. 4.10a. As depicted in fig. 4.10b, the high-resolution spectra of Ni 2p on deconvolution gives rise to 7 peaks with binding energy 853.9, 855.8, 861, 865.45, 871.5, 873.3, and 879.26 eV. The peaks at 853.9 and 871.5 eV corresponds to $2p_{3/2}$ and $2p_{1/2}$ spin-orbit doublets of Ni^{2+}, and the peaks at 855.8, 873.3 eV are attributed to $2p_{3/2}$ and $2p_{1/2}$ orbitals of Ni^{3+} [27, 28]. The presence of satellite peaks (861, 879.26 eV) confirms the II, III oxidation state of Ni. The peak at 865.45 eV in CNOT refers to the satellite peak of Ni $2p_{3/2}$ in NiO [29]. After methanol oxidation, the change in binding energy of the different oxidation states of Ni 2p occurs because of the change in chemical surrounding of the metal ions. The increase in binding energy of Ni^{3+} $2p_{3/2}$ (857.1 eV) and Ni^{3+} $2p_{1/2}$ (874.3 eV) is due to release of electrons from the Ni^{3+} ions. The decrease in intensity of these peaks also suggests the consumption of Ni ions in oxidation of methanol molecules. Furthermore, the decrease in binding energy of Ni^{2+} $2p_{3/2}$ (853.7 eV) and Ni^{2+} $2p_{1/2}$ (864.7 eV) suggests reduction

of the Ni species in the methanol oxidation process. The disappearance of 865 eV satellite peak after methanol oxidation suggests charge transfer from O 2p to Ni 3d orbital of NiO. In fig. 4.10c, the Co 2p spectra exhibits two main peaks at around 780 and 795 eV, arising due to $2p_{3/2}$ and $2p_{1/2}$ orbitals respectively, which on deconvolution give rise to four peaks centred at binding energies 779.6, 781.3, 794.7, and 796.5 eV. Two satellite peaks (787.2, 802.6 eV) appear which confirm the presence of Co^{2+} and Co^{3+} oxidation states. The peaks at 779.6 and 794.7 eV are attributed to Co^{3+} $2p_{3/2}$ and Co^{3+} $2p_{1/2}$, and the 781.3, 796.5 eV peaks confirm the presence of Co^{2+} $2p_{3/2}$ and Co^{2+} $2p_{1/2}$ [13]. Post methanol oxidation, it is found that binding energy of Co^{3+} $2p_{3/2}$ (776.2 eV), Co^{3+} $2p_{1/2}$ (789.9 eV) and Co^{2+} $2p_{3/2}$ (781 eV) get reduced, which implies the increase in electron density on the catalyst's surface due to oxidation of methanol molecules. The change in oxidation states of Co can be inferred from this change in binding energy. The high-resolution spectra of Ti 2p is shown in fig. 4.10d. The peaks correspond to interactions Ti-O $2p_{3/2}$ (458.3 eV) [13, 30], Ti ($2p_{1/2}$)–Ti ($2p_{1/2}$) (459.4 eV) [13], Ti-C 2 $p_{1/2}$ (461.5 eV) [31], C–Ti ($2p_{1/2}$)–T_x (463.65 eV) [30, 32], and 465.07 eV (Ti-O $2p_{1/2}$) [30, 32, 33]. After methanol oxidation the XPS spectra of Ti 2p are observed at 453.08 eV which is due to the Ti-C bond [29]. The other XPS peaks are found at 458.8, 459.4, 459.9, and 465.3 eV which correspond to Ti-O ($2p_{3/2}$), Ti-O, Ti-C 2 $p_{1/2}$, and Ti-O $2p_{1/2}$, respectively. The change in binding energy after methanol oxidation is because of change in chemical environment of the Ti atoms due to the incoming methanol molecules and its oxidation by-products. The decrease in binding energy and intensity of Ti-C peak (461.5 to 459.9 eV) and the disappearance of the 463 eV peak implies the formation of TiO_2. It is corroborated by the increase in binding energy and intensity of Ti-O $2p_{3/2}$ and Ti-O $2p_{1/2}$ interactions (i.e., 458.8 and 465.3 eV respectively). The high-resolution spectra of C 1s spectra reveal four peaks on deconvolution (shown in fig. 4.10e). These 4 peaks are centred at 283.75, 284.76, 285.32, and 287.82 eV which can be ascribed to the interactions C-Ti [27], C = C of sp^2 hybridized carbon, C-OH, and C=O, respectively [15, 27, 30]. The 283.75 eV peak suggests the fact that the structure of MXene do not change after hybridization with $NiCo_2O_4$/NiO. After methanol oxidation these four peaks shift to higher binding energy which is due to the charge transfer from C to its surrounding during the methanol oxidation. Three additional peaks appear at 291.9, 292.21, 293.36 eV after methanol oxidation by CNOT. These peaks are attributed to CHO compound primarily formaldehyde, formate formed as a product of methanol

oxidation [34, 35]. The 285.46 eV is attributed to C-OH; however, it also corresponds to methoxy. As the area of this peak increases after methanol oxidation, it may be due to the presence of these methoxy formed as an intermediate product of methanol oxidation. On resolving the O 1s spectra of CNOT (fig. 4.10f), five peaks centred at 528.9, 529.68, 530.6, 531.7, and 533 eV which arise due to the Ni-O, Co-O, C=O, crystal defect (C-Ti-$(OH)_x$), and adsorbed water molecules, respectively [36].

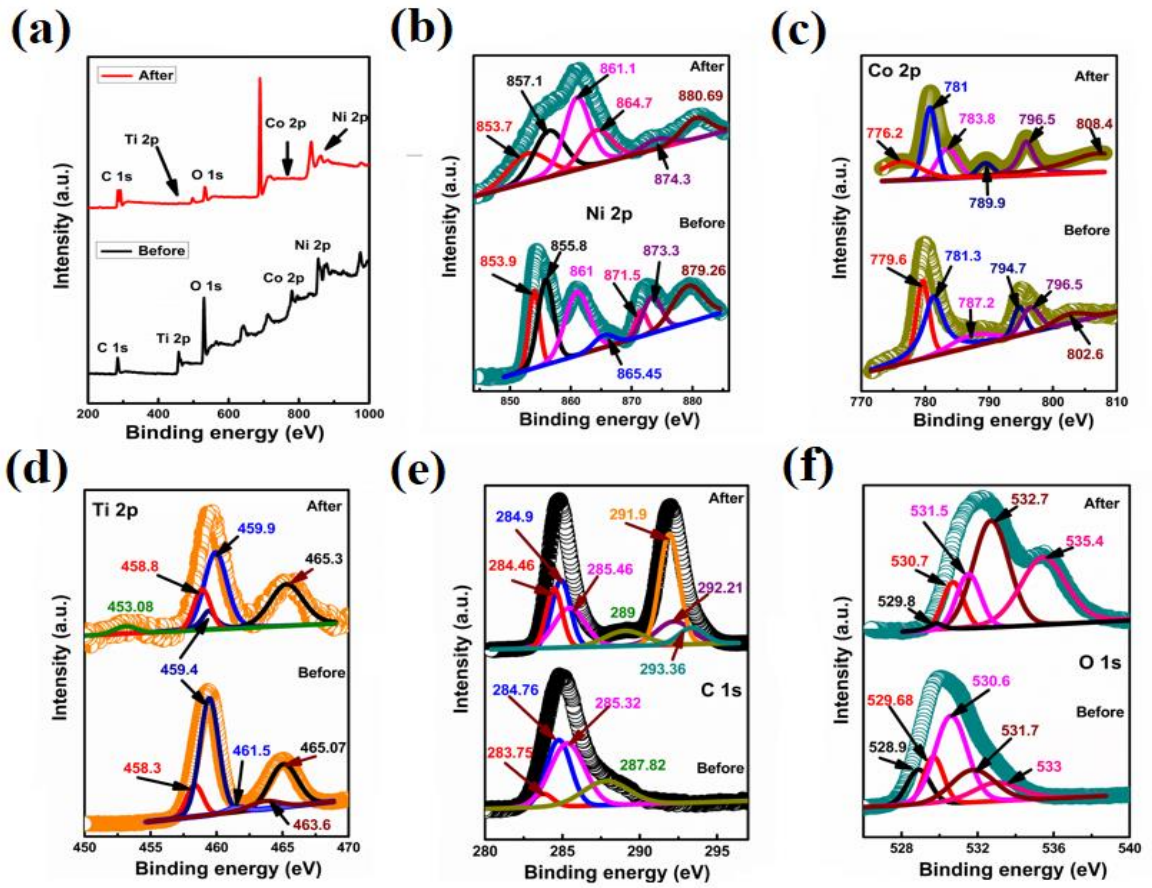

Figure 4.10: (a) XPS spectra of CNOT before and after methanol oxidation: (a) Survey spectra; High-resolution spectra of (b) Ni 2p, (c) Co 2p, (d) Ti 2p, (e) C 1s, and (f) O 1s

The peaks appearing at 529.68 and 530.6 eV also suggests the Ti-O and C-Ti-O_x interactions [13], respectively taking place on the surface of Ti_3C_2 which also corroborates well with the fact that the surface of MXene gets oxidised during its synthesis. The presence of terminal -OH on the surface of MXene can also be inferred from the peak 531.7 and 533 eV. After methanol oxidation, these O 1s peaks get shifted to 529.8, 530.7, 531.5, 532.7, 535.4 eV. The increase in binding energy of Ni-O and Co-O implies the electron transfer, signifying the redox reactions Ni^{2+}/Ni^{3+} and Co^{2+}/Co^{3+}

during the oxidation of methanol molecules. Additionally, the Ni-O peak reduces in intensity which suggests the consumption of Ni in methanol oxidation. It is also observed that the defects and the adsorption of water molecules on the surface of the catalyst CNOT increases which is reflected from the increase in intensity of the peaks. The 535.4 eV also arises due to formaldehyde obtained as by-product of methanol oxidation [37].

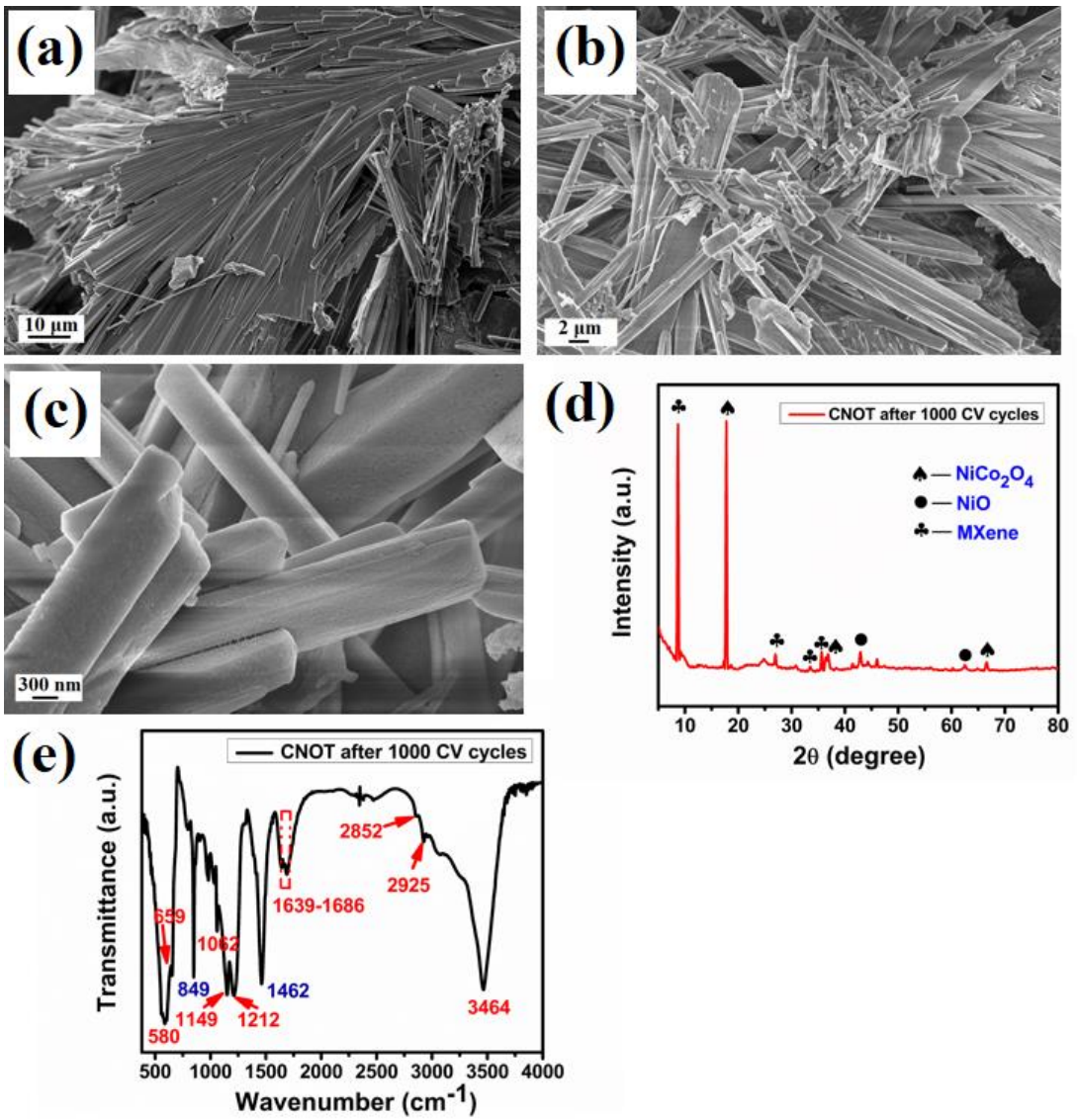

Figure 4.11: Post methanol oxidation characterizations of CNOT: (a)–(c) FESEM micrographs, (d) XRD pattern, and (e) FTIR spectra

To unveil any morphological, crystalline structure changes in the electrode after cycling stability, FESEM and XRD are performed. It is observed from fig. 4.11a, 4.11b, 4.11c that after methanol oxidation for a longer time, MXene sheet loses its layered structure and get restacked. Some of them take the shape of block like structure as can be clearly

visible in fig. 4.11c. The crystalline peaks of CNOT appears with less intensity which may be due to reduction of crystallinity of the sample, disordered restacking or partial reorientation in some specific direction. Increase in intensity of the XRD peak (shown in fig. 4.11d) of MXene at 8.5° may be due to the rolling of the MXene nanosheets, leading to reorientation of the (002) plane in that particular direction. Thus, rolling may lead to the formation of rod-shaped clay like structure as corroborated by the FESEM image in fig. 4.11b and 4.11c. The change in chemical composition of the catalyst is observed by FTIR spectroscopy in fig. 4.11e. Additional absorption peak at 849 cm^{-1} arises due to bidentate carbonate [13]; the band around 1062-1212 cm^{-1} correspond to the bending mode of water, C-O stretching and also appears due to δOH^{-1} of the hydrogen carbonate species formed on the surface of CNOT. Another absorption at 1462 cm^{-1} occurs due to C-O bond and O-H bonding of surface adsorbed methanol molecules. Thus, the surface of the catalyst gets modified by different intermediate products, which decreases the activity after a large number of CV cycles.

4.4 Conclusion

In conclusion, a versatile electroactive material CNOT is developed to explore the synergistic effect of redox-site enriched $NiCo_2O_4$ and NiO, with high surface area, hydrophilicity and conductivity of MXene. FESEM and TEM images reveal the porous layered structure of the nanocomposite. The $NiCo_2O_4$/NiO nanoparticles are decorated over the MXene nanosheets. The mesopores present on hybrid CNOT provide easy insertion of electrolyte ions into the active sites, thus facilitating reversibility to the system. The hydrophilic terminations -O, -F, -OH on the surface of MXene create sites for interfacial interactions with the metal oxides. This interfacial interaction facilitates more charge transfer by increasing the specific surface area and reducing the ion transfer pathways. CNOT exhibits both surface adsorbed and diffusion-controlled mechanisms. The high concentration of surface adsorbed redox sites leads to high methanol current density (15 A/g) with low onset potential (0.30 V vs Ag/AgCl) and low overpotential. Low Tafel slope (88.6 mV/dec), high heterogeneous rate constant (0.9 s^{-1}), and less charge transfer resistance (4.46 Ω) suggest good methanol oxidation ability of the catalyst. The electrode outperforms several carbon-based catalysts by achieving 67% current retention and low degradation rate of 5.85×10^{-6} s^{-1}. The hydrophilic terminations -OH on MXene surface help in adsorbing CO to form CO_2, thereby preventing the

catalyst surface from CO poisoning and recreating the active sites. Thus, high CO tolerance of the catalyst, and almost constant current retention of CNOT after 200 CV cycles suggest electrochemical stability of the catalyst. The change in binding energies of Ni and Co ions reflect the charge transfer taking place during methanol oxidation, which leads to alterations in their oxidation states. Formaldehyde, formate and methoxy are some of the intermediate oxidation products adsorbed on the catalyst surface which are identified by spectroscopic results. The decrease in crystallinity of $NiCo_2O_4$ and NiO implies its active participation in methanol oxidation. After continuous methanol oxidation for 1000 cycles, the MXene sheets get rolled up and some block like structures of the nanocomposite is observed. It reduces the access to active sites for the ions and due to the coverage of the active sites by several carbonate species and water molecules, the methanol oxidation reduces after prolonged use of the catalyst.

4.5 References:

1. Baruah, K., Deb, P. Electrochemically active site-rich nanocomposites of two-dimensional materials as anode catalysts for direct oxidation fuel cells: new age beyond graphene. *Nanoscale Adv*., 3 (13):3681-3707, 2021.
2. Baruah, B., Deb, P. Performance and application of carbon-based electrocatalysts in direct methanol fuel cell, *Mater. Adv*., 2 (16):5344-5364, 2021.
3. Boota, M., Anasori, B., Voigt, C., Zhao, M.Q., Barsoum, M.W. and Gogotsi, Y. Pseudocapacitive electrodes produced by oxidant-free polymerization of pyrrole between the layers of 2D titanium carbide (MXene). *Advanced Materials*, *28*(7):1517-1522, 2016.
4. Ghidiu, M., Lukatskaya, M.R., Zhao, M.Q., Gogotsi, Y. and Barsoum, M.W. Conductive two-dimensional titanium carbide 'clay'with high volumetric capacitance. *Nature*, 516 (7529):78-81, 2014.
5. Zhan, W., Ma, L., Gan, M. and Xie, F. Ultra-fine bimetallic FeCoP supported by N-doped MWCNTs Pt-based catalyst for efficient electrooxidation of methanol. *Applied Surface Science*, 585:152621, 2022.
6. Yan, J., Ren, C.E., Maleski, K., Hatter, C.B., Anasori, B., Urbankowski, P., Sarycheva, A. and Gogotsi, Y. Flexible MXene/graphene films for ultrafast supercapacitors with outstanding volumetric capacitance. *Advanced Functional Materials*, 27 (30):1701264, 2017.

7. Wang, H. and Lee, J. M. Recent advances in structural engineering of MXene electrocatalysts. *Journal of Materials Chemistry A*, 8 (21):10604-10624, 2020.
8. Chandran, M., Raveendran, A., Vinoba, M., Vijayan, B.K. and Bhagiyalakshmi, M. Nickel-decorated MoS_2/MXene nanosheets composites for electrocatalytic oxidation of methanol. *Ceramics International*, 47(19):26847-26855, 2021.
9. Pershaanaa, M., Kamarulazam, F., Gerard, O., Goh, Z.L., Bashir, S., Baruah, K., Deb, P., Ramesh, S. and Ramesh, K. MXenes and Their Transformation to Composites for Potential Applications. *Materials Today Communications*, 35:106143, 2023.
10. Huang, J.J., Liu, X.Q., Meng, F.F., He, L.Q., Wang, J.X., Wu, J.C., Lu, X.H., Tong, Y.X. and Fang, P.P. A facile method to produce $MoSe_2$/MXene hybrid nanoflowers with enhanced electrocatalytic activity for hydrogen evolution. *Journal of Electroanalytical Chemistry*, 856:113727, 2020.
11. Yang, X., Jia, Q., Duan, F., Hu, B., Wang, M., He, L., Song, Y. and Zhang, Z. Multiwall carbon nanotubes loaded with MoS_2 quantum dots and MXene quantum dots: Non–Pt bifunctional catalyst for the methanol oxidation and oxygen reduction reactions in alkaline solution. *Applied Surface Science*, 464:78-87, 2019.
12. Elancheziyan, M., Eswaran, M., Shuck, C.E., Senthilkumar, S., Elumalai, S., Dhanusuraman, R. and Ponnusamy, V. K. Facile synthesis of polyaniline/titanium carbide (MXene) nanosheets/palladium nanocomposite for efficient electrocatalytic oxidation of methanol for fuel cell application. *Fuel*, 303:121329, 2021.
13. Baruah, K. and Deb, P. Enabling methanol oxidation by an interacting hybrid nanosystem of spinel Co_3O_4 nanoparticle decorated MXenes. *Dalton Transactions*, 51 (11):4324-4337, 2022.
14. Zeng, X., Zhao, C., Yin, Y., Nie, T., Xie, N., Yu, R. and Stucky, G.D. Construction of Sandwich-Like $Ti_3C_2T_x$ MXene-$NiCo_2O_4$ Heterostructure for Remarkable Electromagnetic Microwave Absorption. *Available at SSRN 4004901*.
15. Wang, Y., Zhang, Z., Liu, X., Ding, F., Zou, P., Wang, X., Zhao, Q. and Rao, H. MOF-derived NiO/$NiCo_2O_4$ and NiO/$NiCo_2O_4$-rGO as highly efficient and stable electrocatalysts for oxygen evolution reaction. *ACS Sustainable Chemistry & Engineering*, 6 (9):12511-12521, 2018.

16. Zhang, G., Xia, B.Y., Wang, X. and Lou, X.W. Strongly coupled $NiCo_2O_4$-rGO hybrid nanosheets as a methanol-tolerant electrocatalyst for the oxygen reduction reaction. *Advanced materials*, 26 (15):2408-2412, 2014.
17. Wang, F., Wang, Z., Zhu, J., Yang, H., Chen, X., Wang, L. and Yang, C. Facile synthesis SnO_2 nanoparticle-modified Ti_3C_2 MXene nanocomposites for enhanced lithium storage application. *Journal of Materials Science*, 52:3556-3565, 2017.
18. Jiang, H., Ma, J. and Li, C. Hierarchical porous $NiCo_2O_4$ nanowires for high-rate supercapacitors. *Chemical communications*, 48 (37):4465-4467, 2012.
19. Wang, H., Gao, Q. and Jiang, L. Facile approach to prepare nickel cobaltite nanowire materials for supercapacitors. *small*, 7 (17):2454-2459, 2011.
20. Tan, B., Fang, Y., Chen, Q., Ao, X. and Cao, Y. Construction of $Bi_2O_2CO_3/Ti_3C_2$ heterojunctions for enhancing the visible-light photocatalytic activity of tetracycline degradation. *J. Colloid Interface Sci.*, 601:581-593, 2021.
21. Brown, A.P. and Anson, F.C. Cyclic and differential pulse voltammetric behavior of reactants confined to the electrode surface. *Analytical Chemistry*, 49 (11):1589-1595, 1977.
22. Khadke, P., Tichter, T., Boettcher, T., Muench, F., Ensinger, W. and Roth, C. A simple and effective method for the accurate extraction of kinetic parameters using differential Tafel plots. *Scientific reports*, 11 (1):8974, 2021.
23. Li, L. and Xing, Y. Methanol electro-oxidation on Pt-Ru alloy nanoparticles supported on carbon nanotubes. *Energies*, 2 (3):789-804, 2009.
24. Hou, G., Parrondo, J., Ramani, V. and Prakash, J. Kinetic and mechanistic investigation of methanol oxidation on a smooth polycrystalline Pt surface. J. Electrochem. Soc., 161 (3):F252, 2013.
25. Baruah, B. and Kumar, A. PEDOT: PSS/MnO_2/rGO ternary nanocomposite based anode catalyst for enhanced electrocatalytic activity of methanol oxidation for direct methanol fuel cell. *Synthetic Metals*, 245:74-86, 2018.
26. Hao, Y., Wang, X., Zheng, Y., Shen, J., Yuan, J., Wang, A.J., Niu, L. and Huang, S. Uniform Pt nanoparticles incorporated into reduced graphene oxides with MoO_3 as advanced anode catalysts for methanol electro-oxidation. *Electrochimica Acta*, 198:127-134, 2016.
27. Tan, L., Lv, J., Xu, X., Zhao, H., He, C., Wang, H. and Zheng, W. Construction of MXene/NiO composites through in-situ precipitation strategy for dispersibility

improvement of NiO nanoparticles. *Ceramics International*, 45 (5):6597-6600, 2019.

28. Wei, Z., Guo, J., Qu, M., Guo, Z. and Zhang, H. Honeycombed-like nanosheet array composite $NiCo_2O_4$/rGO for efficient methanol electrooxidation and supercapacitors. *Electrochimica Acta*, 362:137145, 2020.
29. Gaskell, K.J., Starace, A. and Langell, M.A. $Zn_xNi_{1-x}O$ Rocksalt Oxide Surfaces: Novel Environment for Zn^{2+} and Its Effect on the NiO Band Structure. J. *Phys. Chem. C*, 111 (37):13912-13921, 2007.
30. Gunasekaran, S., Wang, W. and Yin, Y., Few-Layered Mxene Nanosheets as Peroxidase-Mimic for Colorimetric Detection of Kanamycin. Available at SSRN 4174804.
31. Kannan, K., Sadasivuni, K.K., Abdullah, A.M. and Kumar, B. Current trends in MXene-based nanomaterials for energy storage and conversion system: a mini review. *Catalysts*, 10 (5):495, 2020.
32. Yang, C., Jiang, Q., Huang, H., He, H., Yang, L. and Li, W. Polyelectrolyte-Induced Stereoassembly of Grain Boundary-Enriched Platinum Nanoworms on $Ti_3C_2T_x$ MXene Nanosheets for Efficient Methanol Oxidation. *ACS Appl. Mater. Interfaces*, 12 (21):23822-23830, 2020.
33. Li, J., Liu, Y., Xu, F., Hu, J., Chen, N., Du, G. and Jiang, C. K^+ Intercalation of NH_4HF_2-Exfoliated Ti_3C_2 MXene as Binder-Free Electrodes with High Electrochemical Capacitance. *physica status solidi (a)*, 217 (8):1900806, 2020.
34. Kawashima, A., Asami, K., Hashimoto, K. XPS analysis of amorphous Ni-Nb-Sn-Pt alloy catalysts for electrooxidation of formaldehyde, *Mater. Sci. Eng. A*, 134:1070-1073, 1991.
35. Vohs, J.M. and Barteau, M.A. Conversion of methanol, formaldehyde and formic acid on the polar faces of zinc oxide. *Surface science*, 176 (1-2):91-114, 1986.
36. Narayanan, N. and Bernaurdshaw, N. Reduced graphene oxide supported $NiCo_2O_4$ nano-rods: an efficient, stable and cost-effective electrocatalyst for methanol oxidation reaction. *ChemCatChem*, 12 (3):771-780, 2020.
37. Prosvirin, I.P., Bukhtiyarov, A.V., Bluhm, H. and Bukhtiyarov, V.I. Application of near ambient pressure gas-phase X-ray photoelectron spectroscopy to the investigation of catalytic properties of copper in methanol oxidation. *Applied Surface Science*, 363:303-309, 2016.